Application of computational fluid dynamics codes for nuclear reactor design

YOU Byung-Hyun[1], MOON Jangsik[2], and JEONG Yong Hoon[3]

1. Department of Nuclear and Quantum Engineering, Korea Advanced Institute of Science and Technology, 291, Daehak-ro, Yuseong-gu, Daejeon 34141, Republic of Korea (bhyou@kaist.ac.kr)
2. Department of Nuclear and Quantum Engineering, Korea Advanced Institute of Science and Technology, 291, Daehak-ro, Yuseong-gu, Daejeon 34141, Republic of Korea (moonjaja@kaist.ac.kr)
3. Department of Nuclear and Quantum Engineering, Korea Advanced Institute of Science and Technology, 291, Daehak-ro, Yuseong-gu, Daejeon 34141, Republic of Korea (jeongyh@kaist.ac.kr)

Abstract: Development of computing power allows more sophisticated numerical simulation of single phase heat and mass transfer and makes two-phase simulation more likely. Direct numerical simulation (DNS) of single phase heat and mass transfer is accepted as a reliable replacement of high fidelity experiments with limited scale of the problem. In this paper, various turbulent models are assessed against the DNS to expand the role of computational fluid dynamics (CFD) in the design and analysis of sodium cooled fast reactor core. Also, the benchmarking of Oak Ridge National Laboratory's (ORNL) liquid metal fast breed reactor (LMFBR) experiment is performed for further generation of virtual data to validate system code. This series of validating procedures are introduced as an example of CFD applications to design the high burnup sodium fast reactor.
Keyword: computational fluid dynamics; RANS simulation; core thermal hydraulic design; wire-wrapped fuel pin

1 Introduction

Thermal hydraulic investigation of nuclear reactor core is one of the most important part to design the nuclear power plant. It has been suggested that the helical wire-wrapped fuel assemblies for the coolant mixing. With the helical wire structure generates swept flow over a wire in sub-channels which can affect the temperature and mass flux distribution due to the complex flow behaviors. In series of research for sub-channel analysis of wire-wrapped fuel assembly using commercial CFD codes based on Reynolds average Navier-Stokes (RANS) turbulent model has been studied. Gajapathy *et al.* [1] performed thermal hydraulic analysis of 7-pin wire-wrapped fuel bundle assembly using k-epsilon turbulence model. They investigated velocity distributions of axial and transverse direction and temperature distribution with suggested turbulence friction factor. Extendibility study of 217-pin fuel bundle from the 7, 19 and 37-fuel pin bundles was also performed by Gajapathy *et al.* [2]. On that research, they comparing the friction factor for various Reynolds number against experimental correlation which was done by Novendetern [3]. More recent publications concentrated a quantitative CFD benchmark in terms of velocity, temperature and pressure distribution. (Natesan *et al.* [4], Hamman *et al.* [5] and Fricano *et al.* [6]) Their CFD results were conducted from ORNL in the 1970s. (Fontana *et al.* [7]) Mentioned full sized simulations were evaluating the global tendencies of sub-channel thermal hydraulic characteristics.

The ductless type of fuel assembly was suggested recently in KAIST for high burnup sodium fast reactor which aims to neutron economics. The concept of ductless design is elimination of the wall of hexagonal duct except the six corners for the minimum structure supporting. For determining the design specifications, proper core thermal hydraulic analysis must be simulated using sub-channel analysis code, but the uncertainties of fluid behaviors should be firstly confirmed with reliable reference data. In series of research, CFD validations have been already performed with individual purpose. However, these are only related with conventional type of wire-wrapped fuel assembly not for the ductless concept. In this paper, one possible application of CFD for nuclear reactor design is introduced that design process of

Received date: August 22, 2015
(Revised date: October 12, 2015)

ductless fuel assembly for high burnup sodium fast reactor.

2 Methodology

Multichannel analyzer for steady states and transients in rod array for liquid metal reactors (MATRA-LMR) is a thermal-hydraulic analysis code based on the sub-channel approach for calculating the flow and enthalpy distribution in fuel assemblies and reactor cores for both steady-state and transient conditions. MATRA-LMR has been already validated for the conventional types of fuel assembly [8], however, it should be reconfirmed the potential of the flow mixing and enthalpy distribution for the ductless type fuel assembly. Unfortunately, there is no validation candidate in the same or at least similar case of ductless fuel assembly due to technical difficulties. Therefore, it is necessary to development of the suitable methodology of core thermal-hydraulic analysis for structural change of the conventional core design.

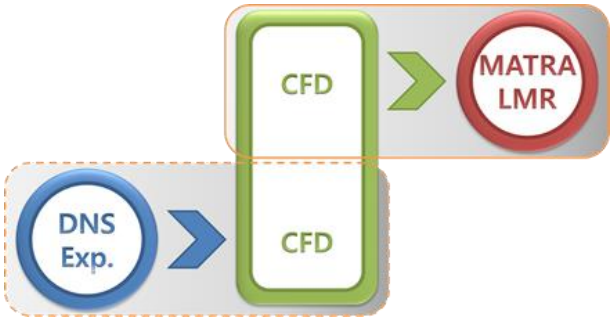

Fig.1 Strategy of system code validation for the conceptual design.

The validation strategy of MATRA-LMR for ductless fuel assembly consists of mainly two validation processes using CFD as a link between real nature and conceptual design as shown in Fig.1. The first step of validation strategy is starting from the turbulent model assessment with high fidelity data from the DNS. The benchmarking of quantitatively well-organized experimental facilities should be performed subsequently. The second step is the virtual data generation, flow mixing and enthalpy distribution of the ductless type of fuel assembly, for MATRA-LMR validation using validated CFD in the first step. The virtual data from CFD is reference data to determining the proper turbulent mixing coefficients for MATRA-LMR in ductless type of fuel assembly. This improved core thermal-hydraulic analysis methodology can be used to design the core thermal-hydraulic for the innovative SFR concept.

3 Assessment of turbulent models

Ranjan *et al.* [9] performed DNS of turbulent swept flow in a stream-wise de-correlated rectangular channel with a wire-wrapped rod bundle as the obstacle structure. This group investigated the turbulent statistics of three-dimensional flow behaviors in a wire-wrapped channel along the axial and perpendicular directions of the wire. The particular locations of the reattachment point and the center of the recirculation bubbles were strongly related to the shear stress layer in four steps of changes in the Reynolds number equivalent flows across the wire. The purpose of this step is assessment of RANS-based turbulence model prediction in turbulent swept flow as a design tool for wire-wrapped fuel assemblies via validation with the DNS results. Standard k-epsilon models with linear and non-linear constitutive relationships and realizable k-epsilon models were chosen as a turbulent model with a two-layer wall treatment approach for observation of the flow behavior.

3.1 Flow description

A rectangular channel with a circular obstacle was provided to match that of the reference DNS calculation. As shown in the Fig.2, the size of the fluid domain is $4\pi h \times 2h \times 8\pi h$ based on the height of obstacle, h, along the x-, y- and z-directions, respectively. Each x-, y- and z-axis denotes the cross-flow direction, vertical direction and the axial direction, respectively. Two pairs of inlet and outlet boundary conditions along the cross-flow direction and stream-wise direction are considered as the periodic boundary, and the other structures are modeled as a no-slip wall boundary of the flow channel. For geometrical modeling of contact between the channel and wire, restrictions exist due to the $180°$ contact angle tangencies. We chose to impose a radial displacement of the circular wire structure in the rectangular flow channel for approximately 2 % of the wire diameter to

avoid numerical errors in the critical line contact region. Pressure gradients of each periodic boundary condition, which result from the adopted constant flow rates in four cases, drive the certain flow and bubble behavior in the channel. In this study, the flow rate of each direction is selected from the reference DNS simulation parameters for a single flow rate in the axial direction with four different and relatively lower flow rates in the cross-flow direction.

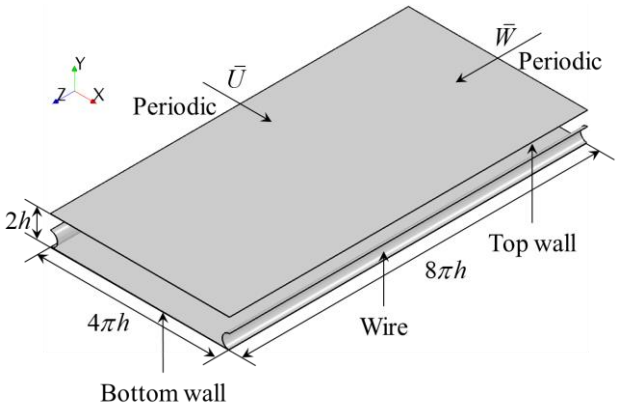

Fig.2 Schematic of the modeled geometry.

3.2 Simulation parameters

The flow is defined by the characteristic velocity and the length scale of each periodic inlet boundary. These characteristic scales are defined by the equivalent Reynolds numbers along the axial direction and cross-flow direction. The flow rates are defined in a general formula based on the channel surface area, *S*, and the average cross-flow and axial flow velocity components *U* and *W*, respectively.

$$Q_z = \iint_S W(x,y)\,dxdy \qquad (1)$$

$$Q_x = L_z \int U(x,y)dy \qquad (2)$$

In the present study, the flow is characterized by the bulk axial velocity W_b and the height of the obstacle structure *h*. Based on these two characteristics of velocity and length scale, the Reynolds number in the axial and cross-flow direction is defined by equation (3) and (4) for each corresponding direction of the bulk velocity, respectively. And the bulk Reynolds number is given by equation (3).

$$Re_z = \frac{\rho W_b h}{\mu} \qquad (3)$$

$$Re_x = \frac{\rho U_b h}{\mu} \qquad (4)$$

$$Re_b = \sqrt{Re_z^{\,2} + Re_x^{\,2}} \qquad (5)$$

In the present study, all cases are adopted from the reference DNS calculation. With an identical axial flow rate equivalent to a Reynolds number of 5,400, four simulations labeled as cases A, B, C and D were defined by varying the flow rates along the cross-flow direction. The equivalent Reynolds numbers of the flow rates for each base are listed in Table 1. In cases A through D, the cross-flow rate is increased to investigate the turbulent statistics of the flow bubble behavior in different situations. Using the characteristic parameters and the formulas, an inverse operation was applied to generate the input of the periodic boundary conditions. Both the cross-flow and axial directional periodic boundary conditions are considered fully developed with a constant mass flow rate and the resulting pressure jump.

To generating the dimensional parameters for the simulation from the given non-dimensional values, we firstly choose the base size of the wire, *h*. In this reference calculation, we selected 1 mm as the wire height which conventional wire diameter size of SFR. After the geometric selection, the axial and crossflow directional bulk velocity could be calculated from the equation (3) and (6), and (4) and (7), respectively. We also selected the temperature to 655 K by adopting from the recommended correlation from SCK-CEN report [10].

$$W_b = Q_z / S \qquad (6)$$

$$U_b = Q_x / (2hL_z) \qquad (7)$$

Table 1 Simulation parameters for all cases

Case	Re_x	Re_z	Re_b	Q_z (ml/s)	Q_x (ml/s)
A	5,400	0	5,400	21.94	0
B	5,400	417	5,416	21.94	3.49
C	5,400	842	5,465	21.94	7.05
D	5,400	1,709	5,664	21.94	14.32

3.3 Computational grid

For proper turbulence modeling, the law of the wall must be satisfied to describe the flow behavior near

the wall surface. To estimate the desired $y+$ for applying the turbulence model, the related variables are calculated from the Reynolds number in the boundary layer in each case. For a turbulent boundary layer over a flat plate, the 99% boundary layer thickness is calculated from the bulk Reynolds number and the channel characteristic length. To adopt the boundary layer thickness, we estimated the Reynolds number in the 99% boundary layer and the skin friction coefficient using the Schlichting skin-friction correlation. Finally, the friction velocity was calculated to generate computational grids that agree with the viscous sub-layer wall treatment model.

In STAR-CCM+, unstructured mesh generation is imposed with various base cell shapes. In the present study, polyhedral mesh and prism layer adaptation was selected as the mesh generation model. Also, the translational periodic interfaces were generated in each direction, and 100% of conformal matching was satisfied for the opposite side (and vice versa). Near the wall boundary, 10 prism layers were stacked for satisfactory resolution in the viscous sub-layer. Overall, $y+$ is less than 1 for the two-layer wall treatment approach. Mesh refinement were performed until reaching the specified accuracy for convergence. In Fig.3, the generated computational mesh alignment is represented on the x-y plane and shows that the above requirement is satisfied.

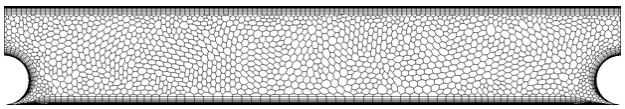

Fig.3 Computational mesh nodes.

3.4 Results

Information on the flow behavior and velocity profiles is provided in this section. Along the cross-flow direction, the particular locations of the reattachment and the center of the recirculation bubble were investigated via projection of streamlines on the x-y plane. The portion of displacement error is defined as the difference between the RANS and the DNS divided total length of crossflow direction.

The tendency of the structure of the recirculation bubble formed by the cross-flow is similar to that of the DNS results. Recirculation bubbles are formed near the leeward side of the wire starting from the top of the wire to a particular location along the cross-flow direction. One major difference from the DNS results is the size of the secondary bubbles between the recirculation bubbles and the leeward side of the wire. In all cases of cross-flow, barely formed secondary bubbles are observed that are similar in size to the bubbles at the opposite side of the wire, which affects the formation of the primary bubbles in terms of the center location of the recirculation zone. The reattachment location is defined as the cross-flow location where the shear stress changes sign, *i.e.*, in the same manner as the DNS reference. For clear comparison with the DNS results, we estimated the particular locations of the points that determine the structure of recirculation bubbles.

The maximum velocities are observed at the top of the wire region for all cross-flow cases due to the acceleration from the leeward side. In the bottom of the recirculation zone, which has a negative or opposite direction, the maximum velocities are shown by the backflows. Figure 4 represents relative crossflow velocity profile in color contour and characteristic locations in the x-y projection which are denoted by x_c, x_t, x_b and x_r, correspond to the center of the channel, top of the wire structure, the center of the recirculation bubbles and the reattachment point, respectively.

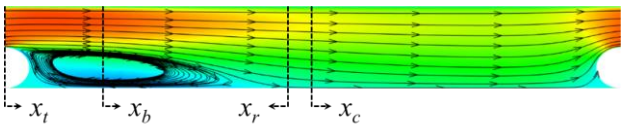

Fig.4 Characteristic locations of flow channel and recirculation bubble structure.

Table 2 represents the particular locations of the recirculation bubble structure and displacements resulting from use of different k-epsilon models compared with the DNS results. All the crossflow directional locations, x_c, x_t, x_b and x_r, are provided in non-dimensional value normalized by height of wire. For the minimum cross-flow rate of case B, the reattachment location is well matched using a

realizable k-epsilon model with 0.88% displacement error. All of the standard k-epsilon models with different constitutive relationships give similar results. In case C, both the linear standard k-epsilon model and the non-linear quadratic standard k-epsilon model satisfactorily predict the recirculation behavior. The errors increase as more complex models are used compared with linear standard k-epsilon model. The maximum cross-flow case is fairly well predicted using the standard k-epsilon model, but the tendency of bubble dispersion is increased using other models.

Table 2 Particular locations of primary recirculation bubble structure and displacement error along the crossflow direction

	Case B			
	x_b	x_r	Error (x_b)	Error (x_r)
DNS	1.39	3.32	-	-
Standard k-ε Linear	1.15	2.71	1.91	4.85
Standard k-ε Quad.	1.15	2.71	1.91	4.85
Standard k-ε Cubic	1.15	2.71	1.91	4.85
Realizable k-ε	1.25	3.21	1.11	0.88
	Case C			
	x_b	x_r	Error (x_b)	Error (x_r)
DNS	2.01	4.67	-	-
Standard k-ε Linear	1.67	4.75	2.71	0.64
Standard k-ε Quad.	1.67	4.75	2.71	0.64
Standard k-ε Cubic	1.68	4.92	2.63	1.99
Realizable k-ε	1.98	6.08	0.24	11.22
	Case D			
	x_b	x_r	Error (x_b)	Error (x_r)
DNS	2.46	5.55	-	-
Standard k-ε Linear	2.01	5.80	3.58	1.99
Standard k-ε Quad.	2.11	6.64	2.79	8.67
Standard k-ε Cubic	2.15	7.27	2.47	13.69
Realizable k-ε	2.52	8.15	0.48	20.69

Mean flow analysis was discussed, as normalized by the characteristic velocity, W_b, along the axial and cross-flow directions. As the cross-flow rate increases from case B to D, the shapes of the axial velocity gradient approach the leeward side of the wire structure. Each turbulence model gives different results in terms of recirculation bubble structures due to the different sensitivities of the anisotropic effect. In cases B, C and D, the minimum errors are observed when using a standard k-epsilon model with linear constitutive relationships.

From an engineering design point of view, the RANS simulation is used to assess the prediction of turbulent statistics due to much lower resource requirements and shorter computation time. In this study, the RANS simulation produced reasonable agreements with the DNS results in terms of mean flow distributions and the recirculation bubble structure. However, the proposed method must be treated carefully as the ratio of the cross-flow rate to the axial flow rate is increased, *e.g.*, a relatively lower mass flow rate than the normal operation condition at the inlet of the fuel assembly. In conclusion, the standard k-epsilon model with a two-layer wall treatment model has sufficient capability to be used in further development of this tool for core thermal hydraulic design with a wire-wrapped fuel assembly.

4 Modeling of fuel assembly

4.1 ORNL LMFBR experiment

The second part of this work is benchmarking the existing experimental facility for re-confirming the design capability of CFD. The ORNL 19-pin bundle experiment [7] was selected which provides numerous data sets and a specification of experimental procedures. As shown in Fig.5, 19-pin fuel rods are arranged by triangular packing within hexagonal can. The axial domain of ORNL test section mainly consists of inlet, heater and outlet sections with 12 in., 21 in. and 3 in. long, respectively. Total 36 grounded or ungrounded thermocouples are located in fluid domain and 9 additional points were observed along the diagonal direction at the exit of channel outlet. They performed 11 types of experiment with each individual purposes that can be simulate various

situations for LMFBR. We selected the reference case, test series 2-test 2-run 109, for normal operation condition with evenly heated pins.

4.2 Quantitative benchmark

Based on the ORNL LMFBR geometry information, we modeled the pin-wire contact by following the results of Merzari *et al.* [11]. They investigated a sensitivity study of pin-wire contact modeling from the point of view of the hydraulics and the heat transfer characteristics based on Ranjan's study. They concluded that the size of contact angle, the nominal gap distance between the wire and wall, does not gives the significant effect for predicting the hot-spot location as long as no flows are exchanged between the wire and wall. For optimizing the mesh, the helically wire-wrapped fuel pin is modeled by 5% radial displacement of wire into the rod to avoiding 180 ° contact angle tangencies. The computational grid were generated based on the automation system in STAR-CCM+. Polyhedral mesh was selected for the bulk of the flow and 5 prism layer added to adopting the wall treatment model. The prism layer size was calculated from our reference case data for satisfying two-layer wall treatment restriction. Base size was chosen to 0.12 mm through a comprehensive mesh study. As discussed in section 3.5, standard k-epsilon with linear constitutive relation model was selected as a turbulence model for the benchmarking.

Observed variables are temperature and pressure drop from the bottom to top of 36 in.-long test section. Figure 7 shows the relative temperature distributions followed by equation (8) at the exit of the channel. The CFD predictions are generally more radical shape comparing to experimental data. However, this tendency should not be interpreted as a limitation of the CFD simulations. J.W. Fricano *et al.* [6] suggested that the majority of error is associated with the position uncertainty of thermocouples. The pink band in Fig.7 represents the coverage of temperature at each channels which contains the experimental results with measurement uncertainty. Temperature comparison to experimental data was performed for the other 36 locations with the same manner of J.W. Fricano *et al.* and the overall error is less than 5% except only 4 points that might be considered as failed thermocouple measurements. From this validation process, we could logically assume that the CFD modeling approach has enough capability to design the further conceptual design based on helical wire-wrapped fuel assembly system.

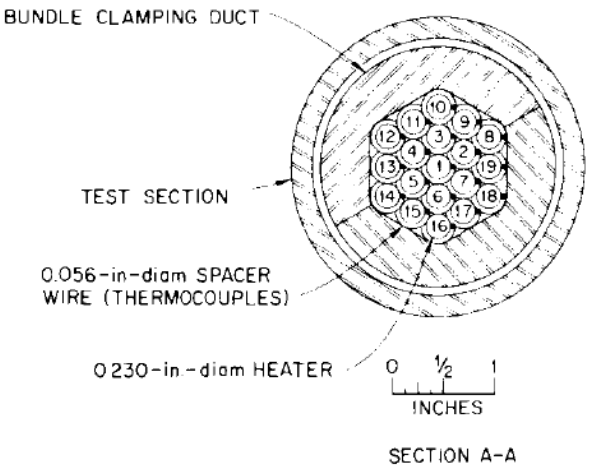

Fig.5 LMFBR FFM 2A test section assembly.

$$Error = \frac{Min_{i=1,2,3}\left(\left|T_{measured} - T_{probe,i}\right|\right)}{T_{measured}} \qquad (8)$$

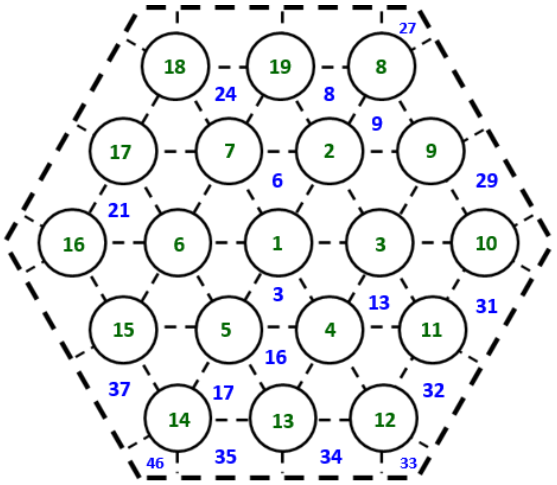

Fig.6 Rod and channel numberings of simulation domain.

4.3 Simulation of ductless fuel assembly

Based on the validated CFD results using assessed turbulence model by DNS, the ductless type of fuel assembly is simulated to generating virtual data for MATRA-LMR validating procedure. The structural reference is also chosen as ORNL LMFBR 19-pin fuel assembly for comparing the effect of the

existence of duct structure. As mentioned in introduction, the duct structure is eliminated except corner section. Total three pairs of transitional periodic boundaries are matched for simulating the flow mixing along the entire flow channel. Firstly we were focused on the differences of temperature distributions at the exit of the outlet channel as shown in Fig.8. In case of ductless type, the tendency of temperature distribution along the diagonal direction is more concentrated at the center of fuel assembly due to relatively large area near the edge of the channel comparing to conventional design.

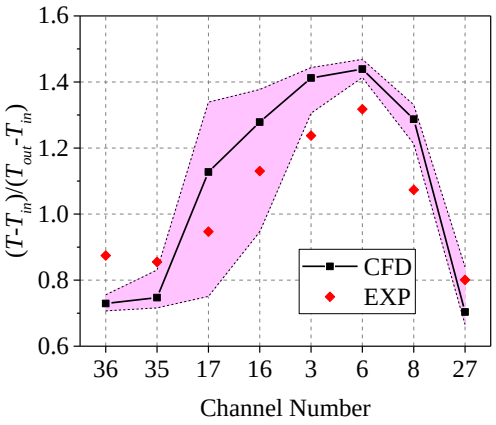

Fig.7 Relative temperature distribution comparison. (ORNL LMFBR experiment vs. CFD).

Finally, MATRA-LMR code was validated with virtual data using CFD for the ductless type of fuel assembly. The major parameter for the validating the code is turbulent mixing coefficient that governing the enthalpy mixing within the sub-channel. This coefficient should be carefully modified whether the errors of temperature distributions are less than certain error boundary or not. Figure 9 shows the relative temperature distributions for ductless type fuel assembly in the same manner as performed in section 4.2. All the values are within the error boundary except channels 35 and 36 which might be considered as the measurement error as discussed. Therefore, we can conclude the MATRA-LMR code can be used without any modifying of turbulent mixing coefficient for ductless type of fuel assembly.

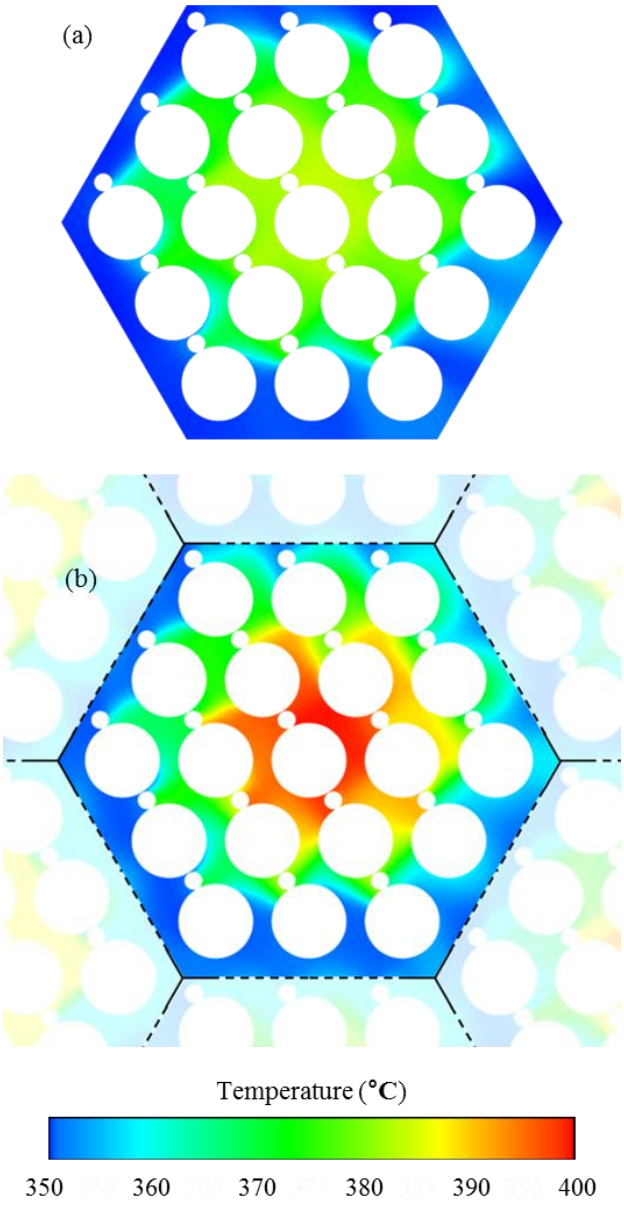

Fig.8 Temperature distributions for (a) a conventional type and (b) a ductless type fuel assembly.

5 Conclusion

In this paper, one possible CFD application for conceptual design of ductless type of fuel assembly is introduced by following the development methodology for generating the virtual data sets using CFD. RANS based CFD is validated with DNS results and ORNL LMFBR experimental data in each separate ways. The standard k-epsilon model shows reasonable agreements to simulating helically wire-wrapped fuel assembly. Further simulation is also performed for ductless type of fuel assembly based on the pre-performed CFD calculations. We could finally conclude that

MATRA-LMR code has enough capabilities for design the ductless concepts without any modifications by comparing properly produced CFD results.

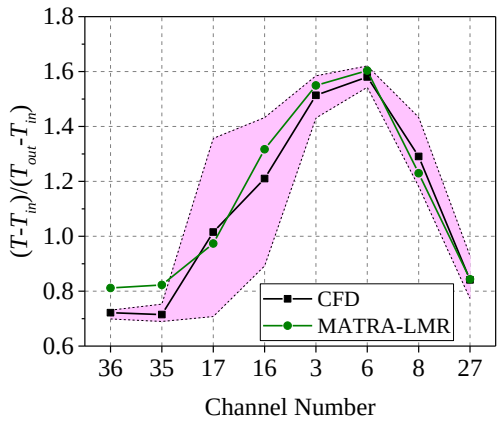

Fig.9 Relative temperature distribution for ductless type fuel assembly.(CFD vs. MATRA-LMR).

Acknowledgement

The authors gratefully acknowledge research support from the National Research Foundation of Korea (NRF) (Grant NRF-2013M2A8A6035681 and NRF-2013M2A8A1041511).

References

[1] GAJAPATHY, R., VELUSAMY, K., SELVARAJ, P., CHELLAPANDI, P., and CHETAL, S.C.: CFD investigation of helical wire-wrapped 7-pin fuel bundle and the challenges in modeling full scale 217 pin bundle, J. Nucl. Eng. Des. 2007, 237:2332-2342.

[2] GAJAPATHY, R., VELUSAMY, K., SELVARAJ, P., CHELLAPANDI, P., and CHETAL, S.C.: A comparative CFD investigation of helical wire-wrapped 7, 19 and 37 fuel pin bundles and its extendibility to 217 pin bundle, J. Nucl. Eng. Des. 2009, 239:2279-2292.

[3] NOVENDSTERN, E. H.: Turbulent flow pressure drop model for fuel rod assemblies utilizing a helical wire-wrap spacer system, J. Nucl. Eng. Des. 1972, 22:19-27

[4] NATESAN, K., SUNDARARAJAN, T., NARASIMHAN, ARUNN, and VELUSAMY, K.: Turbulent flow simulation in a wire-wrap rod bundle of an LMFBR, J. Nucl. Eng. Des. 2010, 240:1063-1072.

[5] HAMMAN, KURT D., BERRY, and RAY A.: A CFD simulation process for fast reactor fuel assemblies, J. Nucl. Eng. Des. 2010, 240:2304-2312.

[6] FRICANO, J. W., and BAGLIETTO, E.: A quantitative CFD benchmark for sodium fast reactor fuel assembly modeling, Ann. Nucl. Energy. 2014, 64:32-42.

[7] FONTANA, M. H., MACPHERSON, R. E., GNADT, P. A., PARSLY, L. F., and WANTLAND, J.L.: Temperature distribution in a 19-rod simulated LMFBR fuel assembly in a hexagonal duct (Fuel failure mockup bundle 2A) - record of Experimental Data, Oak Ridge National Laboratory, Oak Ridge National Laboratory, 1973.

[8] KIM, W. S., KIM, Y. G., and KIM, Y. J.: A subchannel analysis code MATRA-LMR for wire wrapped LMR subassembly, Ann. Nucl. Energy. 2002, 29:303-321.

[9] RANJAN, R., PANTANO, C., and FISCHER P.: Direct simulation of turbulent swept flow over a wire in a channel, J. Fluid Mech. 2010, 651:165-209.

[10] SOBOLEV, V.: Database of thermophysical properties of liquid metal coolants for GEN-IV, SCK-CEN, 2011.

[11] MERZARI, E., POINTER, W.D., SMITH, J.G., TENTNER, A., and FISCHER, P.: Numerical simulation of the flow in wire-wrapped pin bundles: Effect of pin-wire contact modeling, J. Nucl. Eng. Des. 2012, 253:374-386.